Force Sensing Shell using a Planar Sensor for Miniature Legged Robots

Joshua D. Goldberg and Ronald S. Fearing

***Abstract*— Mobile robot contact sensing can be useful for navigation and manipulation with small robots. In this work, we present a low-cost, 18.7 gram force-torque sensor for a 10 cm hexapedal millirobot. A planar array of photointerrupters, rigidly attached to the structure of the robot, is used to measure the six-axis movement of a shell attached to the robot with springs. The sensors measure the intensity of infrared light reflected off of a surface on the underside of the shell, which has been specially designed to enable the resolution of the forces and moments in the x-, y-, and z-axes applied to the shell. The sensor has a force sensitivity of 17 mN and torque sensitivity of 0.72 mN-m for a sampling rate of 100 Hz. The sensor can resolve a force equivalent to 2.9% of the combined robot and sensor weight of 581 mN.**

I. INTRODUCTION

Robots tasked with reconnaissance or search and rescue missions must necessarily be adept at navigating challenging, heterogeneous terrain. As a miniature robot moves through dense vegetation, it is assumed that its body, not just its legs, will be in contact with the environment and experience forces. Analogously, as a small animal moves through foliage, the forces on its body cannot be neglected, and may be more or less significant than the foot forces. It was shown by Li et al. [1] that more terradynamically streamlined shapes in animals and robots can dramatically improve how well they navigate tall blades of grass. Thus, understanding the forces on the body while traversing rich and varied terrain is important for successful locomotion and improving the terradynamics of robots.

There have been several approaches to characterize the environment of a robot by measuring physical interactions during motion. Hair sensor arrays have been used to understand terrain beneath a robot and drag forces [2]. There have been efforts in object detection and wall following as well. Whisker technologies have been developed by Wijaya [3] and Russell [4] as well as instrumented antennae by Lee et al. [5] and Lamperski et al. [6]. To sense tactile forces, Liljeback et al. [7][8] embedded sensors into the joint modules of snake robots to improve locomotion. Commercial six-axis force-torque sensors have also been used between a robot and an encompassing shell, as shown by Tsuji et al. [9].

The Biomimetic Millisystems Lab at U.C. Berkeley is working towards developing low-cost, disposable, bio-inspired millirobots, with masses below 100 grams and lengths on the order of ten centimeters. Thus, heavy, expensive commercial sensors are infeasible for our application. Due in part to the rising ubiquity of the smartphone, a broad assortment of integrated sensors has become widely available. Accelerometers and gyroscopes can be useful for robotic tactile feedback because they can detect impacts, such as running into a wall or an object falling on a robot; they can also detect if a robot becomes inverted.

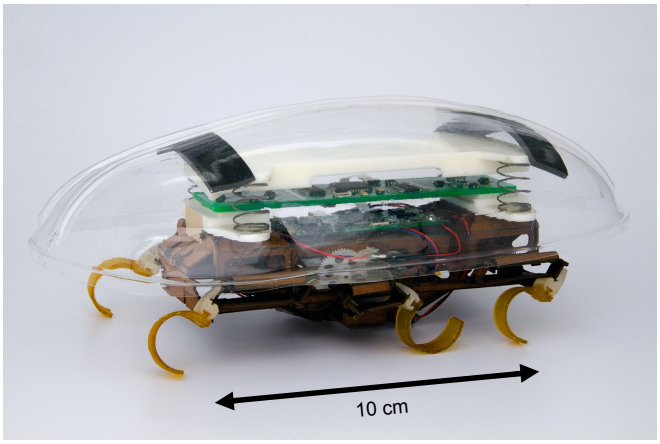

Fig. 1: Force-torque sensor and shell mounted on a VelociRoACH.

However, these sensors cannot measure static loads, and cannot detect, for instance, if the object that fell on the robot continues to trap it, or if it slid off. Thus, a tactile force sensor is required to enable this functionality. Optical proximity sensors have also become cheap and lightweight, and they were used by Hirose and Yoneda [10] to successfully develop a six-axis force-torque sensor. Additionally, Sinden and Boie [11] designed planar capacitive sensors to measure six-axis forces and torques. A planar sensor is of high value, as it can be implemented on a printed circuit board. In this work, a low-cost, lightweight tactile sensor using planar photointerrupters is developed, which is capable of measuring six-axis forces and torques with resolutions on the order of ten millinewtons and five tenths of a millinewton-meter, respectively.

II. METHODS

A. Robot Platform and Technology Overview

The robot used in this work is the VelociRoACH (Fig. 1), a 30 gram, 10 cm long hexapedal millirobot [12]. It is manufactured using the Smart Composite Microstructures (SCM) process [13], which allows the robot to be folded together from planar parts. The VelociRoACH is one of the

This work was supported by the United States Army Research Laboratory under the Micro Autonomous Science and Technology Collaborative Contract W911NF-08-2-0004, and this material is based upon work supported by the National Science Foundation under Grant No. CMMI-1427096.

Joshua D. Goldberg and Ronald S. Fearing are with the Department of Electrical Engineering and Computer Sciences, University of California, Berkeley, CA 94720 USA, jgoldberg@berkeley.edu, ronf@eecs.berkeley.edu

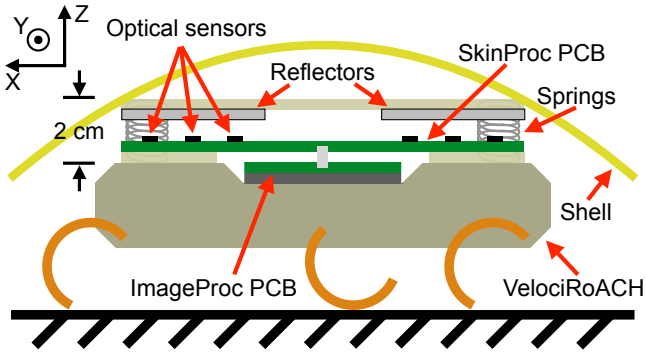

Fig. 2: Side view of sensor and shell mounted on a VelociRoACH, showing optical proximity sensors and sensing springs.

fastest running robots relative to scale, and its design was inspired by the American Cockroach because of the insect's variety of stable, high speed gaits [12].

The VelociRoACH has been modified to carry 18.7 grams of additional hardware for tactile sensing, which is detailed in Fig. 2. The main microcontroller printed circuit board, referred to here as the ImageProc, is responsible for controlling the gait of the robot and recording telemetry data. It communicates with the tactile sensing printed circuit board, referred to in this work as the SkinProc, which is based off previous work by Karras [14]. Photointerrupters surface mounted to the SkinProc (Fig. 3) measure the intensity of light reflected by reflectors attached to four parallel steel springs above the robot. Each spring has a rate of approximately 150 N/m, and is 1.5 cm tall and 1.0 cm in diameter. A 6.7 gram polycarbonate shell is rigidly attached to the reflectors, which has been thermoformed to a 3D printed mold [15]. The forces and torques experienced by the shell are coupled onto the reflector plate, causing displacement that is measured by the photointerrupters on the SkinProc. From this displacement, the six-axis forces and torques on the VelociRoACH's shell are reconstructed.

B. Optical Proximity Sensing

The sensors are commercially available compact photointerrupters (Sharp GP2S60) with a footprint of 5.44 mm^2. The light emitter is a gallium arsenide non-coherent infrared

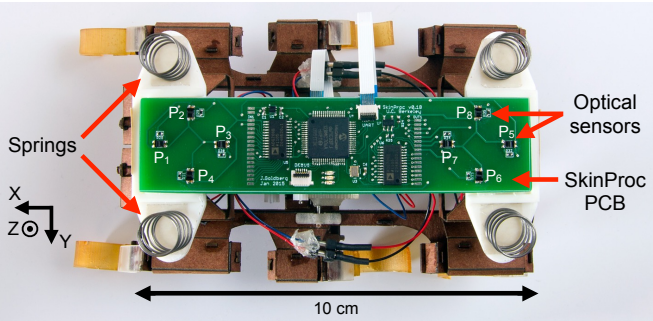

Fig. 3: Photo showing custom SkinProc sensing board with eight proximity sensors mounted in two arrays.

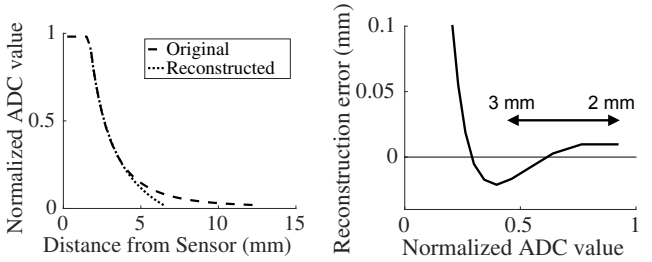

Fig. 4: Response of individual sensor. (a) Proximity sensor response, and $1/r$ fit to curve. (b) Fitting error over 2-5 mm range, with error over most sensitive 2-3 mm range of less than 20 μm.

emitting diode with a maximum emitted wavelength of 950 nm. The light detector is a silicon phototransistor with a maximum sensitivity wavelength of 930 nm. The package has been designed such that the diode and phototransistor are oriented in the same direction, there is no light leakage from the emitter to the detector, and visible light is prevented from exciting the detector. As is shown in Fig. 3, there are eight sensors on the SkinProc, and eight corresponding reflectors on the reflector plate (the design of which is discussed in the following section). The SkinProc contains two 16-channel multiplexers (Analog Devices ADG706) with 100 pA leakage currents and -80 dB crosstalk at 1 MHz. The first multiplexer controls the power supply lines for the emitter-detector pairs and the second controls the detector measurement lines. Thus, it is possible to create an array of up to 16 rows and 16 columns of sensors, and selectively measure only one at a time. For this configuration of eight photointerrupters, only one is powered by each supply line, in order to eliminate the possibility of stray light from an adjacent emitter entering the active detector. The measurement lines feed the current from the phototransistor into a current-to-voltage amplifier, the output of which is read by the 12-bit analog to digital converter of the microprocessor. A full frame of the eight sensor readings is passed to the ImageProc at approximately 100 Hz, which can then be used by the robot to make decisions.

To reconstruct reflector height from sensor output, the least squares method was used to fit a $1/r$ curve to the 2-4 mm range of sensor data. Fig. 4a displays the original data as well as the result of the fit. The fit is very good, with $R^2 > 0.999$ and a worst-case error less than 20 μm for the most sensitive 2-3 mm range, as is shown in Fig. 4b. The linear least squares problem is formulated in Eqn. (1), where s represents the sensor value, r is the range, and a and b are the coefficients that are solved for. Once a and b are found, Eqn. (2) can be used to solve for the reconstructed range $\hat{r}$.

$$s = \begin{bmatrix} \frac{1}{r} & 1 \end{bmatrix} \begin{bmatrix} a \\ b \end{bmatrix}, \tag{1}$$

$$\hat{r} = \frac{a}{s-b}, \tag{2}$$

This method, when used to calibrate all eight sensors of

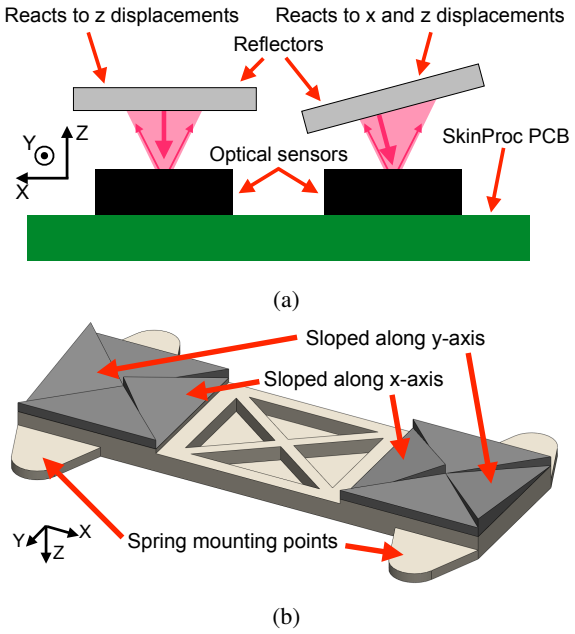

Fig. 5: Principle of operation of force-torque sensor. (a) Spring supported reflective element has sloped reflector geometry that responds to lateral and normal displacement. (b) Complete floating reflective element with 4 reflectors at each end, corresponding to each of 8 proximity sensors.

the SkinProc, enables us to accurately determine the height of each reflector. For static reflector height, there is a standard deviation of only 1 bit in the measurements by the ADC.

C. Reflector Design

Because each sensor can be calibrated to accurately measure the height of the reflector above it, it is then possible to measure the height of a simple reflective plane parallel to the SkinProc moving up and down in the z-axis. In this case, the sensors will not respond to a horizontal displacement of the reflector along the xy-plane because the reflector will remain the same height through the movement. However, if the reflector plane is rotated about the y-axis, as the reflector on the right in Fig. 5a, the height of the point on the reflector directly above the sensor will vary with displacements in both the x-axis as well as the z-axis. The sensor now reacts to two degrees of freedom. This is demonstrated in Fig. 6, where a single panel of reflectors can be designed such that one sensor reacts to lateral displacement along an axis, while the other two sensors stay relatively constant. Building upon this, the eight reflectors were designed to cause the sensors to react orthogonally to motion spanning six degrees of freedom, much in the same way Sinden and Boie were able to arrange capacitors that reacted orthogonally to span six degrees of freedom [11].

The resulting design can be seen in Fig. 5b, where four reflectors are parallel to the xy-plane such that they react to z-axis displacements, two are rotated about the y-axis such that they react to x- and z-axis displacements, and the remaining two are rotated about the x-axis such that they react to y- and z-axis displacements. Using the lengths between sensors and

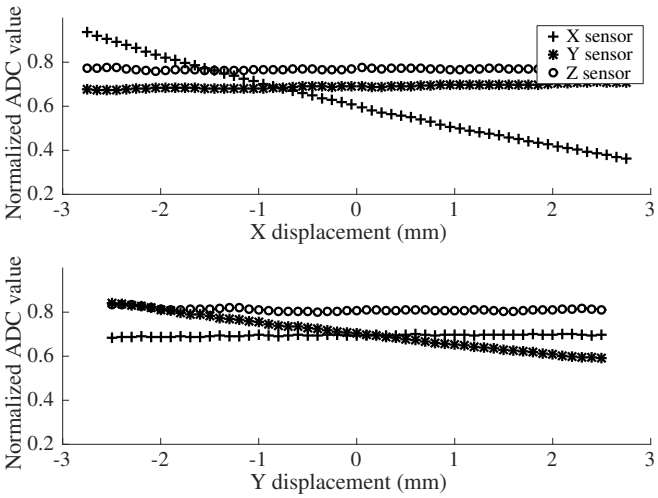

Fig. 6: Sensor displacement test for three sensing elements. Top plot shows response of sensors to x displacement, and bottom plot shows response to y displacement, indicating that sensor responses are relatively independent.

small angle approximations for rotations, there is a linear mapping between the six spatial degrees of freedom and the height that each of the eight sensors would measure with this reflector design. This is seen in Eqn. (3).

$$\begin{bmatrix} R_1 \\ R_2 \\ R_3 \\ R_4 \\ R_5 \\ R_6 \\ R_7 \\ R_8 \end{bmatrix} = \begin{bmatrix} 0 & c_y & 1 & 0 & -l_{15}/2 & c_y{*}l_{15}/2 \\ 0 & 0 & 1 & -l_{24}/2 & -l_{28}/2 & 0 \\ c_x & 0 & 1 & 0 & -l_{37}/2 & 0 \\ 0 & 0 & 1 & l_{24}/2 & -l_{46}/2 & 0 \\ 0 & -c_y & 1 & 0 & l_{15}/2 & c_y{*}l_{15}/2 \\ 0 & 0 & 1 & l_{68}/2 & l_{46}/2 & 0 \\ -c_x & 0 & 1 & 0 & l_{37}/2 & 0 \\ 0 & 0 & 1 & -l_{68}/2 & l_{28}/2 & 0 \end{bmatrix} \begin{bmatrix} x \\ y \\ z \\ \theta_x \\ \theta_y \\ \theta_z \end{bmatrix}, \tag{3}$$

The constants c_x and c_y in Eqn. (3) are the slopes of the reflectors reacting to x- and y-axis displacements, respectively. These are necessary to calculate the change in height seen by the sensor for lateral translations. The l_{mn} constants in Eqn. (3) are the lengths between sensors; for example l_{15} is the length between sensors P_1 and P_5 (sensor numbers are labeled in Fig. 3). The coefficients matrix in Eqn. (3) is rank 6, so its pseudoinverse can be calculated in order to left multiply the column vector of reconstructed heights R_{1-8} to reconstruct the six degrees of freedom. This validates the reflector design in Fig. 5b, because the rank 6 linear mapping confirms that the reflector geometry allows recovery of all displacements and rotations in the xyz-coordinate system.

D. Sensor to Force-Torque Calibration

The previous section shows that the sensor can resolve movement in six degrees of freedom, and thus can be used as a six-axis force-torque sensor. While it would be possible to calculate forces and torques directly from the displacements and rotations of the shell, this would involve a rigorous characterization of the springs as they move in six degrees of freedom with the shell. Instead, work done by Bicchi et

al. [16][17] as well as Voyles et al. [18] was drawn upon to calibrate the force-torque sensor. While recording sensor data from the SkinProc, a commercial force-torque sensor (ATI Nano43) under the VelociRoACH was used to continuously measure a range of forces and torques manually applied to the shell to sweep through most of the input space (because this was done by hand, the forces and torques applied could not be fully exhaustive). Then a polynomial least squares fit was solved between the data from the commercial sensor and the data from the SkinProc. Each set of eight sensor values was arranged as in Eqn. (4) and Eqn. (5), and each set of measured force-torque values was arranged as in Eqn. (6).

$$s_1^* = \begin{bmatrix} s_1 & s_1^2 & s_1^3 \end{bmatrix}, \tag{4}$$

$$S = \begin{bmatrix} s_1^* & s_2^* & \dots & s_8^* \end{bmatrix}, \tag{5}$$

$$M = \begin{bmatrix} F_x & F_y & F_z & M_x & M_y & M_z \end{bmatrix}, \tag{6}$$

The least squares equation was formulated with $n = 97526$ samples, as in Eqn. (7) and Eqn. (8). A pseudoinverse as in Eqn. (9) was used to solve for C, the 24x6 calibration matrix that maps sensor data to forces and torques.

$$M = SC, \tag{7}$$

$$\begin{bmatrix} M_1 \\ M_2 \\ \vdots \\ M_n \end{bmatrix} = \begin{bmatrix} S_1 \\ S_2 \\ \vdots \\ S_n \end{bmatrix} C = \begin{bmatrix} S_1 \\ S_2 \\ \vdots \\ S_n \end{bmatrix} \begin{bmatrix} c_{1,1} & \dots & c_{1,6} \\ c_{2,1} & \dots & c_{2,6} \\ \vdots & \ddots & \vdots \\ c_{24,1} & \dots & c_{24,6} \end{bmatrix}, \tag{8}$$

$$C = (S^T S)^{-1} S^T M, \tag{9}$$

III. Results

A. Force-Torque Estimation

The calibration step was performed with $n = 97526$ samples, the calibration data set. To create this calibration data set, forces between about ± 1 N and torques between about ± 60 mN-m were applied manually and slowly to the shell in all axes while the SkinProc proximity sensor values and the forces and torques from the commercial sensor were recorded. This input range was used to prevent the sensor from saturating. This data set was used to generate the sensor response matrix, C in Eqn. (9), to be used to map proximity sensor values to forces and torques. Another data set was gathered, the test data set, which was a non-exhaustive set with $n = 42316$ samples. The test data was also created with manually applied forces between about ± 1 N and torques between about ± 60 mN-m. The sensor response matrix was then applied to the proximity sensor values of the test data set to estimate the forces and torques applied to the shell.

These estimates are compared directly to the true values from the commercial sensor in Fig. 7 for each of the three forces and three torques. For each force and torque, the majority of the data points fall in a relatively tight band around the dashed line with slope of 1, which indicates an ideal 1-to-1 linear mapping. There are indeed some obvious outliers, which speak to the fact that the sensor is not perfect for all forces and moments applied to the shell. However, it is not expected to be the case that this cheap, lightweight sensor would have the accuracy and precision of an expensive commercial force-torque sensor like the one used in the calibration step. Thus, it is tolerable to have a small degree of error in the force-torque estimates.

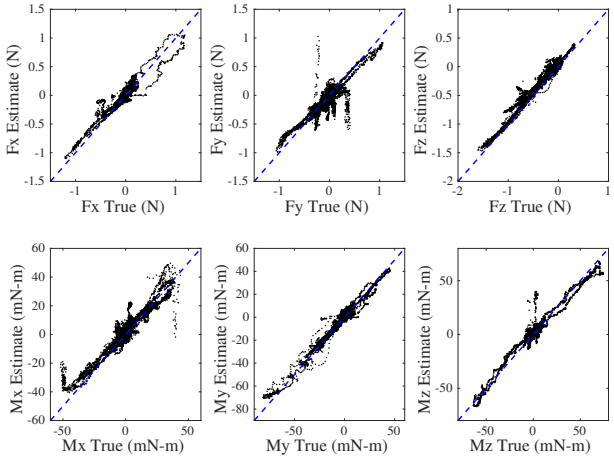

Fig. 7: Measured and reconstructed force-torque data compared directly. Time is eliminated in order to visualize the linearity of the mapping over a range of forces and torques. The dashed lines have slopes of 1, indicating an ideal 1-to-1 linear mapping.

Table I shows the median percent error between true and estimated forces and torques for each axis of the test data set. Because the error distributions become skewed as a result of very large percent errors that arise when the true force is almost zero, these medians are calculated for individual force magnitudes above 0.2 N and torque magnitudes above 10 mN-m (a 0.2 N force applied 5 cm away from the axis of rotation). Table I also shows the worst case error for each axis as a percentage of the maximum range applied to the given axis in the test data set.

The fit method previously discussed has only been verified for the experiments detailed in the following sections. There is also a small constant offset for certain axes, thus an average is used to zero the measurements.

TABLE I: Median percent error and worst case error as a percentage of range for the estimated forces and torques for the test data set (n=42316).

	F_x	F_y	F_z	M_x	M_y	M_z
Median percent error	18%	18%	16%	15%	7.6%	11%
Worst case error	20%	59%	25%	43%	19%	28%

B. Gravity Vectors

To further analyze the performance of the system, the force vector measured by the SkinProc was compared to the acceleration vector measured by the accelerometer on the ImageProc. Theoretically, these two vectors should be aligned parallel with gravity when no other acceleration is enacted on the robot. To test this, a 50 gram mass was rigidly attached to the top of the shell of the VelociRoACH and data was collected while the robot was rotated clockwise around its x- and y-axes slowly at a constant velocity to

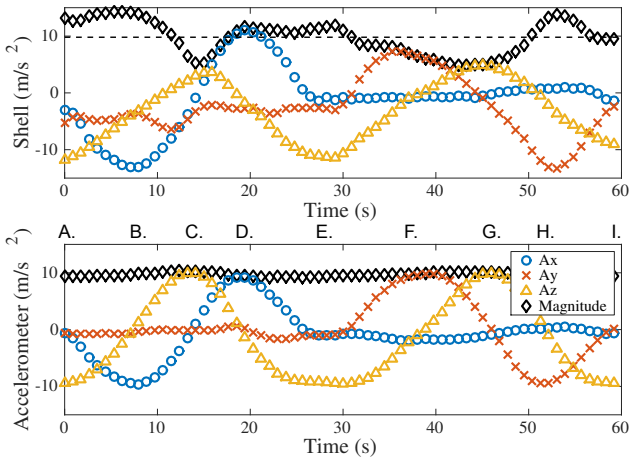

Fig. 8: A comparison of the acceleration traces measured by both the shell and the accelerometer on board the VelociRoACH. The robot is slowly rotated first clockwise around its y-axis and then clockwise around its x-axis. Each letter marks a different orientation of the robot in the rotation sequence: A. legs down; B. nose up; C. legs up; D. nose down; E. legs down; F. left side down; G. legs up; H. left side up; I. legs down.

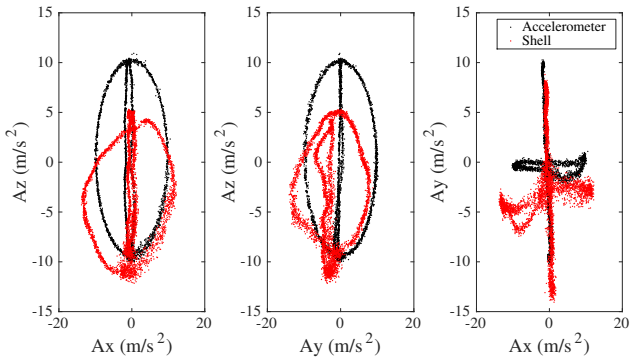

Fig. 9: Slices of the three-dimensional acceleration vector space for the data from both the accelerometer and the shell through the rotation sequence of the robot.

not expose the robot to any acceleration besides gravity. As the robot was rotated first around its y-axis and then around its x-axis, the acceleration traces of both the shell and the accelerometer follow approximately the same paths, as is apparent in Fig. 8. The acceleration measured by the shell here was calculated by dividing the reconstructed forces by the 50 gram mass (solving for a in Newton's second law of motion $F = ma$). Because the calibration step did not take into account extensive data for upward forces on the shell, the system reports about half the correct acceleration when the robot is inverted. This is more apparent in Fig. 9, which shows slices of the three-dimensional acceleration vector space. Here, the shell underestimates the force of gravity when it is inverted, which is illustrated by the Az component of the shell only reaching about 5 m/s^2 instead of 9.8 m/s^2. Despite the errors in the force reconstruction, dividing the force vector magnitude by the acceleration vector magnitude yields a mean mass of 50.4 grams. Thus, moving through

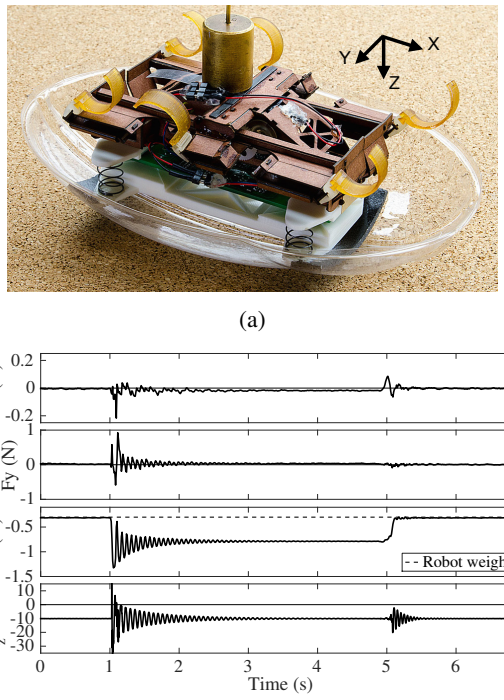

(a)

(b)

Fig. 10: Step response of sensor to a 50 gram mass. (a) Photo of VelociRoACH on its back with a 50 gram mass resting on its underside. (b) Three-axis force data and z-axis accelerometer data for a 50 gram mass placed on the robot at 1 second and removed at 5 seconds.

a variety of orientations, on average the robot is able to successfully measure the load on its shell. Additionally, the reconstructed accelerations follow the accelerometer traces reasonably well, with a mean error angle between the two vectors of 18.8 degrees. Therefore without an accelerometer, the robot would still be able to determine the approximate direction of the gravity vector acting on it using data from the shell alone.

C. Step Response

A step response experiment was used to determine how quickly the sensor would respond to weight being added to the robot, as well as the accuracy of the measurement. In Fig. 10a, the VelociRoACH can be seen inverted with 50 grams resting on its underside. The mass was dropped onto the robot from a height of about 0.5 cm, and lifted off four seconds later. The reconstructed forces as well as z-axis accelerometer data are plotted in Fig. 10b. Ringing is apparent at approximately 15 Hz, resulting from the spring-mass-damper system. The soft springs give large displacements, enabling good sensitivity at the cost of this oscillatory behavior. In future work, damping will be implemented to reduce shell ringing.

The z-axis accelerometer data demonstrates that an impact occurred at $t = 1$ second, however it is unclear from this data whether or not the object remained on the robot. Upon inspecting the reconstructed F_z data, it is apparent that for the period from 1-4 seconds, there is a force of about -0.5

N on the robot, which is approximately the force of a 50 gram mass. Using this method, the sensor fit was validated for masses up to 150 grams placed on the robot in the z-axis, and up to 70 grams in the x- and y-axes.

D. Collision Detection

To demonstrate operation of the force-torque sensor during locomotion with contact, the robot was run into obstacles as shown in Fig. 11a. The corresponding forces, leg positions, and integrated z-axis gyroscope data for the VelociRoACH are in Fig. 11b. This experiment had multiple stages. For section [I], in which the robot is at rest, the measured forces are nominally static and zero, as expected. Once the robot starts walking with a stride frequency of 2 Hz, as indicated in the leg position data, the force data begins to oscillate in synchrony with this motion, bounded by ± 0.15 N. In section [II] when the robot collides with the corner, there is a negative spike in F_x and F_y of approximately -0.2 N. The signs of these forces are expected, because the collision occurs on the front-left corner of the shell, causing the robot to turn to the right. This is also substantiated by the θ_z gyroscope data in section [II] of Fig. 11b. In section [III], a negative F_y was expected as a result of the robot repeatedly contacting the wall on its left side. However, the sensor forces and torques indicate the possibility of complex dynamic contacts during this interval which merit further study (see attached video). In section [IV], the sensor measures a sharp spike of -0.5 N for F_x, a result of the perpendicular collision between the robot and the wall. The sign and magnitude of this force are as expected, since the shell is displaced along the negative x-axis in the collision, and the magnitude is equal to the maximum thrust force the 0.7 N robot can produce, approximately 0.5 N. This was calculated using the coefficient of static friction of the robot on corkboard, $\mu_s = 0.7$, which varies with leg position. For the following 2 seconds as the robot continues to collide with the wall, the F_x data oscillates with a period of 2 Hz (the stride frequency) between -0.2 N and -0.5 N, which identifies and measures the repeated collision. The force data corresponding to the complicated motion and contact conditions in Fig. 11 demonstrates the utility of the sensor, and the potential for the VelociRoACH to not only detect collisions, but also characterize the contact forces involved.

IV. CONCLUSIONS

A planar sensor was developed using photointerrupters and a reflector surface which partially decouples motions in order to measure the forces and torques applied to the shell of a millirobot. This sensor will enable the robot to better interact with its environment by providing intelligence about the objects it encounters with good sensitivity, as seen in Table II, which compares the sensing ranges and resolutions of the SkinProc to those of a commercial sensor. Most of the robot interactions that are of interest to detect, such as differentiating between pushing another robot and against a wall, fall outside the 3 standard deviation sensitivity range, thus enabling reliable detection. For example, the standard deviation of F_x is 5.4 mN, and a static collision force is up to 0.5 N. These detection algorithms will be developed and implemented in future work. Also, the calibration method can be improved in order to reduce force estimation error, so that the contact location of the force on the shell can be calculated. New shell designs need to be explored that shield the sensor from stray infrared light and encompass the entire robot body in order to seal it from dirt, as in Haldane et al. [15], as well as to enable the detection of high-centering or to measure the ground drag force.

TABLE II: Range and resolution of force-torque sensors. Each cell of the table is displayed as range/resolution.

	F_x (N)	F_y (N)	F_z (N)
SkinProc	2.3/.0054	2.1/.0167	1.9/.0051
ATI Nano43	18/.0039	18/.0039	18/.0039
	M_x (mN-m)	M_y (mN-m)	M_z (mN-m)
SkinProc	96/0.72	127/0.25	138/0.44
ATI Nano43	250/0.05	250/0.05	250/0.05

ACKNOWLEDGMENT

We thank Carlos Casarez for his guidance through the robot manufacturing process as well as providing the shell used on the robot, Jaakko Karras for his previous version of the SkinProc PCB and codebase, and Dr. Chen Li for plotting the data from Fig. 11 in real time with the experiment video, as seen in the attached media. We thank Andrew Pullin for his calibration advice, his assistance with media collection and editing, and his generosity with time and wisdom. We thank the members of the Biomimetic Millisystems Lab at U.C. Berkeley, as this work could not have been possible without their guidance and support.

REFERENCES

[1] C. Li, A. O. Pullin, D. W. Haldane, H. K. Lam, R. S. Fearing, and R. J. Full, "Terradynamically streamlined shapes in animals and robots enhance traversability through densely cluttered terrain," *Bioinspiration and Biomimetics*, vol. 10, no. 4, p. 046003, 2015. [Online]. Available: http://stacks.iop.org/1748-3190/10/i=4/a=046003

[2] J. Karras, D. Haldane, and R. Fearing, "Rapid-manufacturable hair sensor array for legged millirobots," in *IEEE/RSJ Int. Conf. on Intelligent Robots and Systems*, Oct 2012, pp. 1956–1962.

[3] J. Wijaya and R. Russell, "Object exploration using whisker sensors," in *Australasian Conf. on Robotics and Automation*, Nov 2002, pp. 180–185.

[4] R. Russell and J. Wijaya, "Object location and recognition using whisker sensors," in *Australasian Conf. on Robotics and Automation*, Dec 2003.

[5] J. Lee, S. Sponberg, O. Loh, A. Lamperski, R. Full, and N. Cowan, "Templates and anchors for antenna-based wall following in cockroaches and robots," *Robotics, IEEE Transactions on*, vol. 24, no. 1, pp. 130 –143, Feb 2008.

[6] A. Lamperski, O. Loh, B. Kutscher, and N. Cowan, "Dynamical wall following for a wheeled robot using a passive tactile sensor," in *IEEE Int. Conf. on Robotics and Automation*, April 2005, pp. 3838 – 3843.

[7] P. Liljeback, K. Pettersen, and O. Stavdahl, "A snake robot with a contact force measurement system for obstacle-aided locomotion," in *IEEE Int. Conf. on Robotics and Automation*, May 2010, pp. 683–690.

[8] P. Liljeback, O. Stavdahl, K. Pettersen, and J. Gravdahl, "A modular and waterproof snake robot joint mechanism with a novel force/torque sensor," in *IEEE/RSJ Int. Conf. on Intelligent Robots and Systems (IROS)*, Oct 2012, pp. 4898–4905.

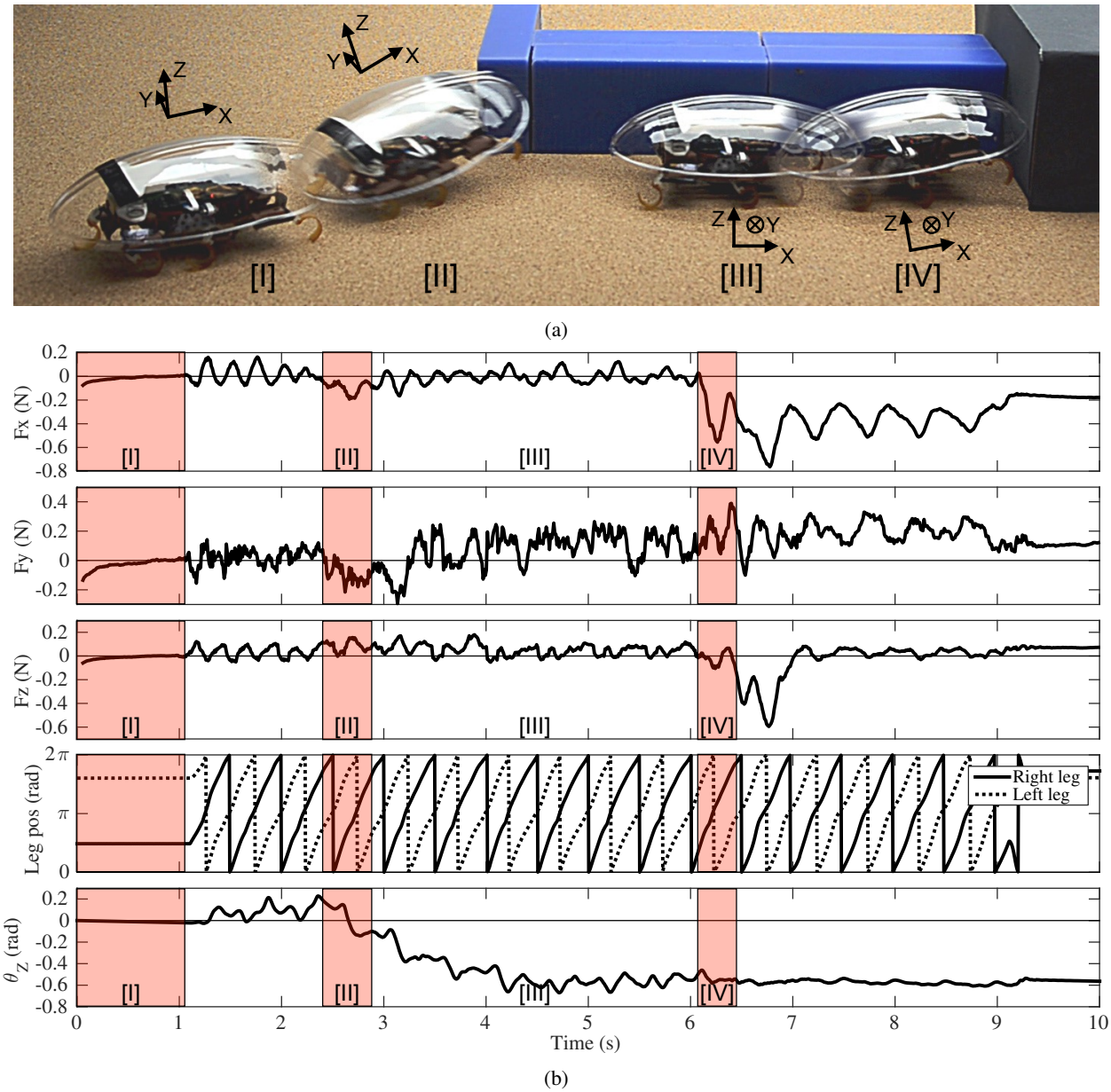

Fig. 11: The VelociRoACH in (a) is shown stationary [I], running into a corner [II], following a wall [III], and colliding with a perpendicular wall [IV]. The corresponding x, y, and z forces, as well as the right and left leg positions and the integrated z-axis gyroscope data are shown in (b).

[9] T. Tsuji, Y. Kaneko, and S. Abe, "Whole-body force sensation by force sensor with shell-shaped end-effector," *Industrial Electronics, IEEE Transactions on*, vol. 56, no. 5, pp. 1375–1382, May 2009.

[10] S. Hirose and K. Yoneda, "Development of optical six-axial force sensor and its signal calibration considering nonlinear interference," in *IEEE Int. Conf. on Robotics and Automation*, May 1990, pp. 46–53 vol.1.

[11] F. Sinden and R. Boie, "A planar capacitive force sensor with six degrees of freedom," in *IEEE Int. Conf. on Robotics and Automation*, vol. 3, Apr 1986, pp. 1806–1814.

[12] D. Haldane, K. Peterson, F. Garcia Bermudez, and R. Fearing, "Animal-inspired design and aerodynamic stabilization of a hexapedal millirobot," in *IEEE Int. Conf. on Robotics and Automation*, May 2013, pp. 3279–3286.

[13] A. Hoover and R. Fearing, "Fast scale prototyping for folded millirobots," in *IEEE Int. Conf. on Robotics and Automation*, May 2008, pp. 886–892.

[14] J. Karras, "Tactile sensors for palm-size crawling robots," Master's thesis, EECS Department, University of California, Berkeley, May 2014. [Online]. Available: http://www.eecs.berkeley.edu/Pubs/TechRpts/2014/EECS-2014-40.html

[15] D. W. Haldane, C. S. Casarez, J. T. Karras, J. Lee, C. Li, A. O. Pullin, E. W. Schaler, D. Yun, H. Ota, A. Javey, and R. S. Fearing, "Integrated manufacture of exoskeleton and sensing for folded millirobots," *Journal of Mechanisms and Robotics*, vol. 7(2), 2015.

[16] A. Bicchi, "Intrinsic contact sensing for soft fingers," in *IEEE Int. Conf. on Robotics and Automation*, May 1990, pp. 968–973 vol.2.

[17] A. Bicchi, J. K. Salisbury, and D. L. Brock, "Contact sensing from force measurements," *The International Journal of Robotics Research*, vol. 12, no. 3, pp. 249–262, 1993.

[18] R. M. Voyles, J. D. Morrow, and P. K. Khosla, "The shape from motion approach to rapid and precise force/torque sensor calibration," *Journal of dynamic systems, measurement, and control*, vol. 119, no. 2, pp. 229–235, 1997.